Nanoscale

Accepted Manuscript

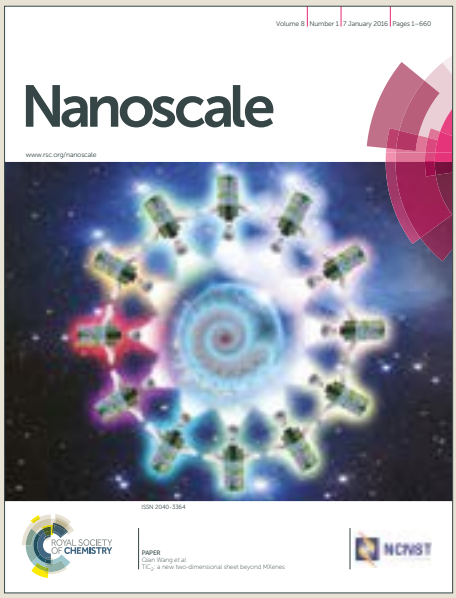

ROYAL SOCIETY OF CHEMISTRY

rsc.li/nanoscale

View Article Online
DOI: 10.1039/C7NR04466F

Nanocrystals generated under tensile stress in metallic glasses with phase selectivity

Yancong Feng,[ab#] Wei-Bing Liao,[ac#] Jiaxin Zheng,[a] Lin-Wang Wang,[d]* Yong Zhang,[e]* Jianfei Sun[f] and Feng Pan[a]*

[a]School of Advanced Materials, Peking University, Shenzhen Graduate School, Shenzhen 518055, China

[b]South China Academy of Advanced Optoelectronics, South China Normal University, Guangzhou 510006, China

[c]College of Physics and Energy, Shenzhen University, Shenzhen 518060, China

[d]Materials Science Division, Lawrence Berkeley National Laboratory, Berkeley, California 94720, United States

[e]State Key Laboratory for Advanced Metals and Materials, University of Science and Technology Beijing, Beijing 100083, China

[f]School of Materials Science and Engineering, Harbin Institute of Technology, Harbin 150001, China

* Corresponding author.

E-mail: lwwang@lbl.gov (Lin-Wang Wang); drzhangy@ustb.edu.cn(Yong Zhang); panfeng@pkusz.edu.cn (Feng Pan).

[#]These authors contributed equally.

View Article Online
DOI: 10.1039/C7NR04466F

ABSTRACT: Revealing the mechanism of phase selectivity can provide the guidance for controlling the crystals with certain phase for special property. In present work, nanocrystals in sizes of about 2–4 nm diameters with the B2 structure (thermodynamic metastable phase) are generated from the CuZr glassy fiber by applied tensile stress at ambient temperature. Combined the ab initio calculations with the molecular dynamics simulations, the stabilities of B2 austenite and B19' martensitic phases under applied tensile stress are compared, and the phase transformation mechanism is revealed. The results present that the B2 structure has a bigger attractive basin, and phase transition could occur with a larger applied stress during the deformation. Therefore, the insight of the higher symmetric B2 nanocrystal with selectivity nucleation driven under directional stress is demonstrated.

Keywords: Nanocrystallization; Metallic glasses; Phase selectivity; Phase transition; Tensile stress

View Article Online
DOI: 10.1039/C7NR04466F

1. Introduction

Over the past half century, metallic glasses (MGs) have attracted considerable attentions for their unique and excellent mechanical, chemical and physical properties,[1-4] but their room-temperature brittleness has been the stumbling block for real structural applications.[5, 6] Many efforts have been made to improve their ductility at room temperature, and the CuZr-based bulk metallic glasses (BMGs) system has been one of the most classic and effective systems to realize this achievement.[7, 8, 25] In the CuZr-based BMGs, the stress can induce nanocrystallization and martensitic transformation and lead to the observed strain hardening and ductility. However, the mechanism of the phase transition and selectivity is still unclear.

It has been confirmed that crystals embedded in the metallic glasses can promote the mechanical performance of material.[8] CuZr-based alloys, which have very good glass forming ability,[9, 10] have been proved to be interesting for the study of crystallization and phase transformation.[11] The B2 austenite CuZr can significantly enhance the fracture strain and decrease the yield strength under compressive loading.[12] The work hardening of the B2 phase is attributed to the martensitic transformation from B2 austenite to B19' martensite CuZr during the plastic deformation.[13] However, in our study it was found that B19' phase was unstable and could transform into B2 phase at lower tensile stress. Therefore, revealing the mechanism of phase selectivity can provide the guidance for controlling the crystals with certain phase through special treatments, such as annealing[14] and preloading.[15]

Due to the importance of austenite phase, several mechanisms of

View Article Online
DOI: 10.1039/C7NR04466F

over-stabilization of the austenite phase have been proposed, such as interfacial energy contribution mechanism,[16, 17] internal defect contribution mechanism[18, 19] and strain-contribution mechanism.[20-22] For the temperature-induced phase transformation, the austenite phase shears into twin-related variants of the product with martensite phase during the cooling process.[23] Addition of the third element can stabilize the B2 CuZr phase during quenching.[24] For the stress-induced phase transformation, the previous experimental observations focused on the B2→B19' martensite transformation of CuZr alloy in the plastic region of tension,[25] whereas the theoretical calculations mainly studied the evolution of the topology structure.[10, 26] The mechanism of phase selectivity induced by stress still remains unclear.

In present work, we observed the crystallization in CuZr metallic glass with phase selectivity under tensile stress. Furthermore, theoretical calculation was used to understand the mechanism of phase selectivity during the deformation.

2. Materials and methods

2.1. Experimental procedure

To investigate the phase transformation mechanism precisely, the same composition of $Cu_{50}Zr_{50}$ alloy with two different sample sizes were chosen in our experiments. Due to the different cooling rates, different phase structures were obtained. The cast fibers at micro-scale are fully amorphous, comparing with a few crystalline phases formed in the rod samples, which are good and convincing carriers for the study. Alloy ingots with a nominal composition of $Cu_{50}Zr_{50}$ (at. %) were

View Article Online
DOI: 10.1039/C7NR04466F

prepared by arc-melting a mixture of elements with a purity level of ＞99.9% in a Ti-gettered high purity argon atmosphere. The cylindrical rods with a diameter of 5 mm were prepared by copper-mold casting under argon atmosphere. And the fibers were fabricated by the melt-extraction method (MEM). The edge angle of the Cu wheel (diameter about 200 mm) was fixed at 60°. The circumferential velocity V_w of the Cu wheel was 30 ms^{-1}. In the apparatus, the position of the cylindrical rods by induction melting could be controlled. The molten mother alloy was extracted by moving up the melt cylindrical rods under a high purity argon atmosphere, and forming a fine, rapidly cooled circular fiber with a high surface-to-volume ratio.[27] The surface morphologies and actual fiber diameters were examined in a Zeiss SUPRA 55 scanning electron microscope (SEM). The phase structures of the rod and wires were examined by X-ray diffraction (XRD) with Cu Kα radiation. The thermal properties were analyzed by differential scanning calorimetry (DSC) (NETZSCH STA 449) at a heating rate of 20 K/min.

Tension experiments were conducted on an Instron 5848 microtester with a gauge length of ~20 mm and a strain rate of 8.33×10^{-5} s^{-1} at ambient temperature. The test fibers were bonded to a specially designed paper frame with a rhombic hole at the center by the epoxy adhesive. When the testing sample was fixed on the cross-head, the paper frame was cutoff through the middle. The tensile stresses were calculated using the force values of the tensile experiment divided by the sample cross-section at the point of failure observed in the SEM. The microstructures of the samples were examined by high resolution transmission electron microscopy (HRTEM) using a

View Article Online
DOI: 10.1039/C7NR04466F

TECNAI-F30 instrument operated at 300 kV. To reduce the impact of focus ion beam (FIB) and HRTEM, the samples were cooled by liquid nitrogen during preparation, and the observation time of the sample under electron beam is very short.

2.2. Computational details

For the comparison of attractive basins and the thermodynamic analysis, density functional theory (DFT) calculations were performed using the projector-augmented wave methods implemented in the Vienna ab initio simulation package (VASP). The Perdew-Burke-Ernzerhof (PBE) form of the generalized gradient approximation (GGA) was selected as the exchange-correlation potential. The plane wave energy cutoff was set to 520 eV. The maximum residual force was less than 0.02 eV/Å. The k-point mesh was set to be $3\times3\times3$. The B2 ($3\times2\sqrt{2}\times2\sqrt{2}$ unit cells) and B19' ($3\times2\times2$ unit cells) supercells were built.

To intuitively observe the phase transition, molecular dynamics simulations for dynamic analysis were adopted to study the phase transition under uniaxial strain, using the code LAMMPS. The embedded-atom method (EAM) potentials[28] were used. The NPT ensemble is employed, and the temperature is fixed at $T=300\,\mathrm{K}$ by using the Nose-Hoover thermostat. Periodic boundary conditions are adopted in all three directions. The velocity-Verlet algorithm is applied to integrate the equations of motion with a time step 1 fs. B2 ($15\times10\sqrt{2}\times10\sqrt{2}$ unit cells) and B19' ($15\times10\times10$ unit cells) supercells were built. Both supercells contain 6000 atoms, with a side length of about 4–5 nm, which is larger than the diameters (2–4 nm) of the nanocrystals observed in the experiments. Though the number of atoms is small, it is

View Article Online
DOI: 10.1039/C7NR04466F

enough in our crystalline model, judging by the smooth stress–strain curves and clear visual snapshots during the phase transition. After achieving the energy minimization relaxation, the systems were stretched, and the strain rates were $5\times10^{8}\ s^{-1}$.

3. Results

3.1. Nanocrystallization with B2 phase under tensile stress

The formation of nanoscale structure of a material depends on the temperature and cooling history.[29] In this study, samples with different diameters and cooling rates were prepared, and the final microstructures of alloy were observed by transmission electron microscopy (TEM) at the ambient temperature. To reduce the impact of the electron beam, the observation time of the sample under TEM is very short. **Fig. 1**(a) shows the $Cu_{50}Zr_{50}$ rod with a diameter of 5 mm by vacuum suction method (Supporting Information, section SI.1). According to the cooling rate equation studied by W.L. Johnson,[30] the cooling rate of the rod sample was estimated to be ~10^2 K/s. The X-ray diffraction (XRD) patterns of the rod shown in **Fig. 1**(b) prove that there are two phases of B2 and B19' crystals in the glassy matrix after quenching. **Fig. 1**(c) shows the HRTEM image of the phase microstructures in the rod. The potential energies of the B2 and B19' phases are closed ($\Delta E = 0.022$ eV atom^{-1}, Supporting Information, section SI.1), thus they can coexist in the glassy matrix.

View Article Online
DOI: 10.1039/C7NR04466F

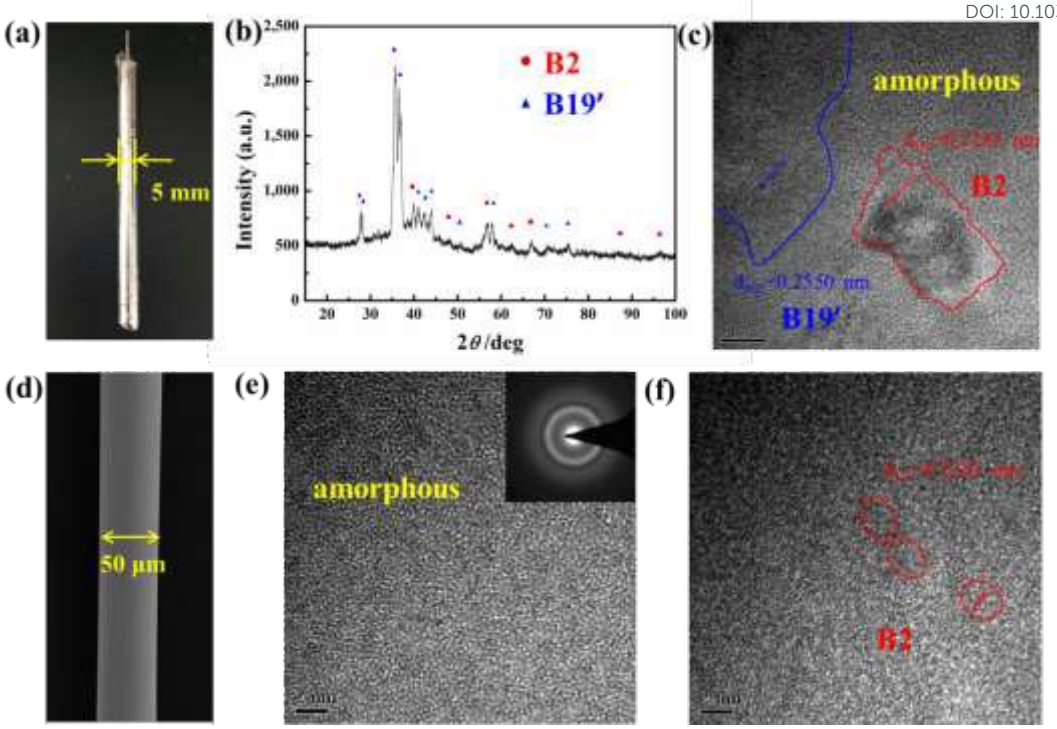

Fig. 1. Generation of nanocrystals in $Cu_{50}Zr_{50}$ alloy during the quenching and under tensile stress. (a) Sample of $Cu_{50}Zr_{50}$ rod with a diameter of 5 mm. The XRD patterns (b) and the HRTEM image (c) of $Cu_{50}Zr_{50}$ rod after slow quenching (~10^2 K/s). (d) The surface morphology of $Cu_{50}Zr_{50}$ fiber with a diameter of 50 μm. (e) The HRTEM image of the fiber after fast quenching (~10^6 K/s). (f) The HRTEM image of the fiber after tension.

The melt-extracted glassy fiber samples with a diameter of 50 μm were prepared, and the corresponding cooling rate was increased to ~10^6 K/s (Supporting Information, section SI.2) as shown in **Fig. 1**(d), in which the magnified microscopic image shows that the micron-sized fiber is axially and radially uniform with a smooth surface. The HRTEM microstructures for the fiber specimens are presented in **Fig. 1**(e), which shows no hint for the presence of any distinguishable crystallites. The selected area

View Article Online
DOI: 10.1039/C7NR04466F

electron diffraction pattern from the overall structure also shows only amorphous rings. Though very tiny nanocrysllines could be found to be randomly present in the glassy matrix in the bulk $Cu_{50}Zr_{50}$ metallic glasses,[7] the glassy fiber is much thinner, and has a faster cooling rate to avoiding any crystallization during fabrication. Meanwhile, the results of XRD with a very slow scanning rate and differential scanning calorimetry (DSC) further prove that fiber sample is fully amorphous after cooling, shown in Fig.S4 (Supporting Information, section SI.2). Significant changes of the structure at the scale of several nanometers can be observed in the HRTEM images after tensile stress is applied, where the strain is within $\varepsilon = 1.20\,\%$. As metallic glasses generally have a large elastic strain limit of ~2%,[2-4] the deformation with a strain of 1.20% is much less than the elastic strain limit. A small amount of B2 nanocrystals, with an average size of 2 nm starts to appear in the amorphous matrix, as shown in **Fig. 1**(f). The generation of nanocrystals in CuZr metallic glassy fibers, induced by uniaxial tensile stress with a strain value of $\leq$ 2% is very interesting, as nanocrystallization induced by deformation itself is a plastic procedure. The HRTEM images exhibit that the lattice fringes are in good accord with the plane distances of the B2 phase. We noticed that only the B2 phase was formed during the tension of the amorphous fibers, suggesting that the B2 phase compared with the B19' phase is much easily formed under tensile stress.

View Article Online
DOI: 10.1039/C7NR04466F

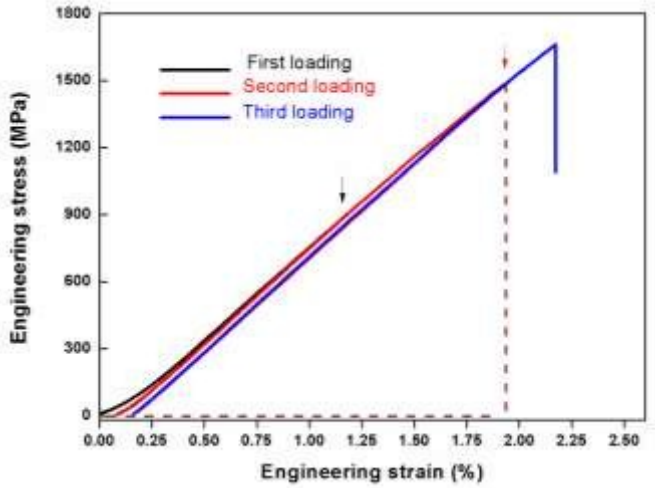

Fig. 2. Room temperature tensile engineering stress-strain curve of the metallic glassy fiber sample loaded three times before attaining its final fracture.

To explore the formation of these nanocrystals induced by tensile stress in the micron-sized metallic glassy fiber, we have carried out a multiple-loading tension experiment on the sample. The loading cycle consisted of loading up to a few per cent of strain followed by the complete unloading and was applied three times. The corresponding engineering stress-strain curve is presented in **Fig. 2**. It can be observed that the strain never returns to zero during unloading, and upon subsequence reloading, the stress-strain relationship followed the unloading curve and returned to the same stress and continued the deformation with further loading. However, the elastic modulus of the fiber has slightly increased during the second and third reloading. This deviation indicates that the microstructure of the metallic glassy fiber has changed under tensile stress. According to Wagner,[31] crystallization in MGs always implies significant change in the local elastic modulus and atomic configuration on the short- to medium-range length scale can be perfectly icosahedral

View Article Online
DOI: 10.1039/C7NR04466F

which exhibits similar or even higher modulus values compared to the long-range crystal. For the micron-sized metallic glassy fiber, B2 nanocrystals can be easily formed from the amorphous matrix under tensile stress, thus leading to the slight increment of the elastic modulus.

3.2. Comparison of attractive basins of the B2 and B19' structure under stress

To explain this experimental phenomenon and in-depth understanding the phase selectivity mechanism between B2 and B19', we have applied the ab initio calculations and molecular dynamics simulations to study the phase stability under stress. Firstly, the basins of the attraction of the B2 and B19' structure under stress were compared. In order to study the possible paths for phase transformation between the B2 and B19' crystals, and to mimic the effects of strain and stress, we have gradually changed the lattice parameters between B2 and B19'. More specifically, the lattice of primitive cell is transformed gradually and uniformly to another phase in 10 steps, while keeping the internal coordination of the atoms. This is followed by atomic relaxation of the internal atomic coordinates while to keep the periodic cell geometry fixed. The resulting energies are shown in **Fig. 3**(a). We then relax the whole system including the cell geometry. When the initial cell geometry is in the B2 phase with the condition of only the internal atomic coordinates to be relaxed, the system will stay in a high energy state but not in the B19' phase state, for comparison while the cell geometry to be allowed to relax, the system will relax back into the B2 state, proven by the X-ray intensities calculation shown in **Fig. 3**(b).

View Article Online
DOI: 10.1039/C7NR04466F

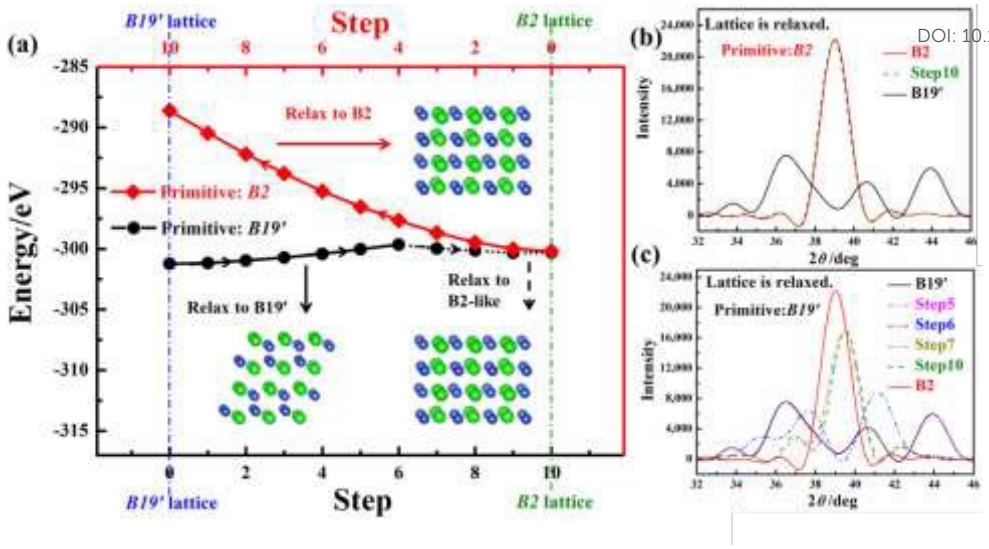

Fig. 3. Evolutions of system energies during the transformations between the B2 ($3\times2\sqrt{2}\times2\sqrt{2}$ unit cells) and B19' ($3\times2\times2$ unit cells) lattices, calculated by the ab initio. The lattices were changed gradually and uniformly in 10 steps, and the corresponded energies after internal atomic relaxations were shown (a). The lattice at each step was then relaxed. (b and c) X-ray intensities calculation with primitive structures B2 and B19', respectively.

The inverse process is done with the initial cell geometry in the B19' phase. For this time, when the cell geometry passes step 6, the whole system will relax to a B2-like phase, while before step 6, the system will return back the B19' structure. The B2-like structure can be proven by the X-ray intensities calculation (**Fig. 3**(c)). The evolution of the phase structure in this process can be also verified by the topological structures, calculated by Voronoi Indexes,[32] which are shown in **Table 1**.

Table 1. Voronoi Indexes of alloy during the deformation from the B19' lattice to the B2 one.

View Article Online
DOI: 10.1039/C7NR04466F

	Lattice is fixed.		Lattice is relaxed.	
	Cu-center	Zr-center	Cu-center	Zr-center
B19'	<2, 3, 0, 6>	<0, 5, 2, 10>	<2, 3, 0, 6>	<0, 5, 2, 10>
step 1~6	<0, 5, 2, 5>	<0, 5, 0, 9>	<2, 3, 0, 6>	<0, 5, 2, 10>
step 7~10	<0, 6, 0, 8>	<0, 6, 0, 8>	<0, 6, 0, 8>	<0, 6, 0, 8>
B2	<0, 6, 0, 8>	<0, 6, 0, 8>	<0, 6, 0, 8>	<0, 6, 0, 8>

The results of these calculations indicate that the B19' structure can be irreversibly transformed to the B2 structure, but B2 structure is difficult to be transformed into the B19' structure. Thus the B2 structure has a much larger basin of attraction, despite of the fact that the B19' has a slightly lower energy under the ambient pressure. Larger attractive basin means B2 phase is easier to be formed and more stable under uniaxial stress. Though the B19' nucleus may generate after quenching, they would transfer to the B2 phase. Thus, only B2 nanocrystals were found after tension.

3.3. Thermodynamic analysis of the phase transition from B19' to B2

The above calculation studies the attractive basins of different phases, especially after an applied stress is released. Now we further study this issue from the thermodynamic point of view using ab initio calculation. As shown in **Fig. 3**(a), at the ambient pressure, the B19' phase has slightly lower energy. However, the situation can change under stress. The thermodynamic phase transitions under hydrostatic pressure are well studied.[33, 34] Under pressure P, the thermodynamic property which

View Article Online
DOI: 10.1039/C7NR04466F

determines the crystal phase is not the energy E, but the enthalpy $H = E + PV$, where the V is the volume of the cell. The situation for uniaxial stress is more complicated. Under tensile stress, we can assume that there is no crystal orientation rotation, but only small deformations. Thus, we have applied uniaxial tension in the three crystal lattice directions of the crystal phase B19'. Under each stress ε, we find a mostly likely path of crystal cell change, gradually from B19' to B2, which can both release the energy but also have a smooth path. Thus the difference of the enthalpy ΔH between the B19' and B2 phases under this uniaxial stress will equal to their energy difference $E_2 - E_1$ under this stress, and the work W to change the cell shape from B19' to B2. In other word:

$$\Delta H = E_2 - E_1 + W \qquad (1)$$

where E_1 and E_2 are the internal energies of phase 1 and phase 2 under stress ε (i.e., both deformed B19' and B2 cells under ε), and work W if the cell is changed from phase 1 to phase 2, which can be written as (see Ref. 35)

$$W = P_x \int_1^2 l_y l_z dl_x + P_y \int_1^2 l_x l_z dl_y + P_z \int_1^2 l_x l_y dl_z \qquad (2)$$

where l_x, l_y and l_z are the x-, y-, z-direction lattice length, and P_x, P_y, P_z are uniaxial pressure (stress) in the x-, y-, z-directions. Under uniaxial tension (Z-direction), P_x and P_y are zero. Therefore, the principle for the phase transition can be written as

$$\Delta H = E_2 - E_1 + P_z \int_1^2 l_x l_y dl_z \le 0 \qquad (3)$$

Fig. 4(a) shows the result of calculated ΔH for the phase transition from B19' to B2. The uniaxial phase transition pressures in the Y-direction and Z-direction are

View Article Online
DOI: 10.1039/C7NR04466F

1.557 GPa and 1.382 GPa, respectively. With our experiment of strain 1.20%, the corresponding stress is 0.9 GPa, which is smaller than the transition stress for the Y- and Z-directions. Nevertheless, given the uncertainty intrinsic to the ab initio calculations, and possible small clusters of the B19' phase in the amorphous matrix, the actual transition stress could be smaller. Overall, our simulation indicates that under an applied tensile stress, there could be a thermodynamic tendency for some of the B19' phases (at some orientations) to change to B2 phase. The structural analysis during the phase transition is discussed. **Fig. 4**(b) shows the snapshots of B19' and B2 structures at $\Delta H = 0$, where the uniaxial tension was added in the Y-direction. The arrows show the moving directions of the atoms, which is proven by the coordinates and the internal forces of atoms (Supporting Information, section SI.4). At $\Delta H = 0$, the stress imposed on the B19' and B2 structures are equivalent. However, the internal forces of atoms in B19' structure with lower symmetry exhibit much greater than that in B2 structure with higher symmetry. The mechanical behavior of metallic materials is strongly reliant on their electronic structures;[36-38] hence, the charge density differences are presented for the analysis on the quantum scale, shown in **Fig. 4**(c). The yellow region represents electron accumulation, meaning the formation of bond. For the B19' structure, the anisotropy of electron redistribution further indicates the direction of force of atoms. Once the B19' transforms to the B2, the electron redistribution exhibits the isotropic behavior. The results show that the phase transition is accompanied with the improvement of symmetry.

View Article Online
DOI: 10.1039/C7NR04466F

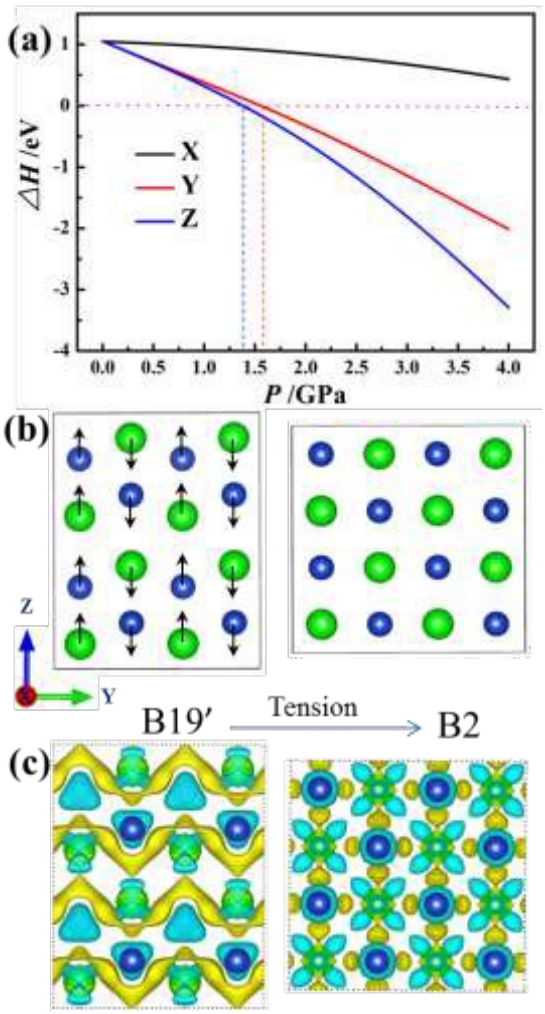

Fig. 4. Thermodynamic analysis of the phase transition from B19' to B2, using ab initio calculations. (a) Variations of enthalpy with increasing tensile stresses. The B19' ($3\times2\times2$ unit cells) lattices were uniaxially stretched in three directions, respectively. During the uniaxial tensile, the lateral directions of lattice were relaxed. (b) Snapshots of B19' and B2 structures at $\Delta H=0$, where the uniaxial tension was added in the Y-direction. The arrows show the moving directions of the atoms if the phase transition occurs. (c) Charge density differences ($\Delta\rho=\rho(\mathrm{CuZr})-\rho(\mathrm{Cu})-\rho(\mathrm{Zr})$) of B19' and B2 structures at $\Delta H=0$. The yellow and cyan regions represent electron accumulation and depletion, respectively. The isosurface value is 0.005 e/Å^3. Blue and green atoms are Cu an Zr, respectively.

View Article Online
DOI: 10.1039/C7NR04466F

3.4. Dynamic analysis of the phase transition between B2 and B19' under uniaxial strain

Although thermodynamics ultimately determines the equilibrium phase in the certain condition, whether and how the nanostructured phase is produced depends on kinetic processes.[39] We here also study this problem from a pure dynamic growth. Due to the nonuniformity of internal stress, the phase transition can start from some local region where the force is sufficiently large, or some nucleation happens. Such small crystalline regions can grow into large crystals. Similarly, for phase transition from one phase to another, one can initially assume a small crystal domain embedded in another crystal matrix, and monitor how this domain grows with time or stress. To intuitively observe such evolution of phase transition, we have adopted the MD simulations, using embedded-atom method (EAM) potentials.[28] The alloys were imposed with uniaxial tensile in the Y-direction. As the number of atoms must be large enough for the study of the deformation behaviors in MD simulations, the 6,000-atoms and 48,000-atoms system were compared (Supporting Information, section SI.5). The results of the two systems are almost the same. Thus the 6,000-atoms system is enough for our simple crystalline model. In order to clearly observe the evolution of the phase transition, we selected the smaller system (6,000-atoms) with a size closed to the nanocrystals observed in the experiments. **Fig. 5** presents the stress-strain behaviors and the evolutions of structures during the uniaxial tensile in the Y-direction. As the strain increases, the stress σ of system rises to a critical value and then drops, as shown in **Fig. 5**(a,b). The declined region is

View Article Online
DOI: 10.1039/C7NR04466F

the phase transition zone, as shown by the snapshots in **Fig. 5**(c,d), and proven by radial distribution functions shown in **Fig. S10**.

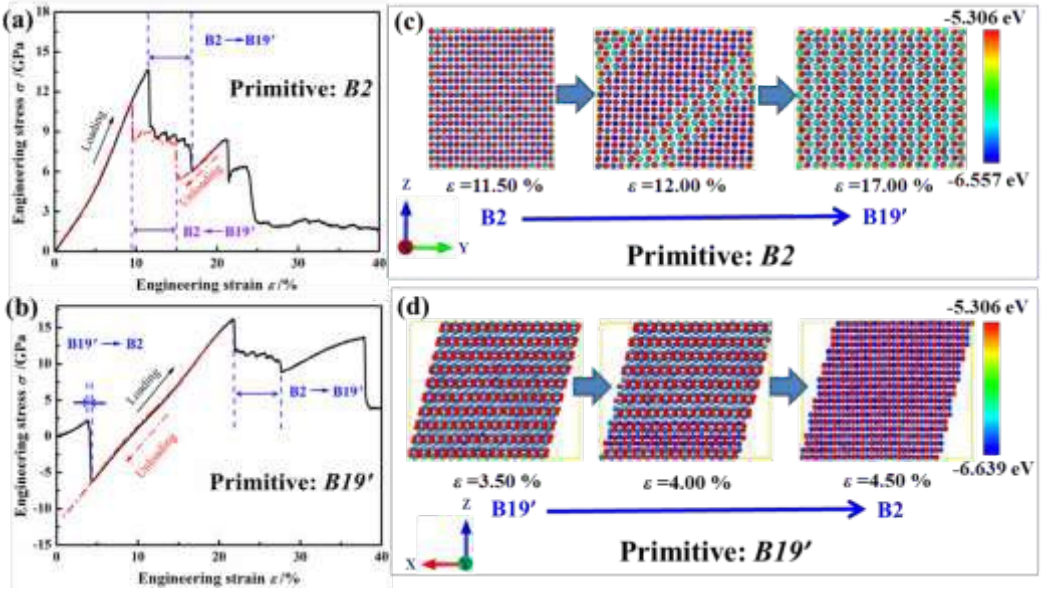

Fig. 5. Room-temperature tensile stress–strain curves of (a) B2 ($15\times10\sqrt{2}\times10\sqrt{2}$ unit cells) and (b) B19' ($15\times10\times10$ unit cells) structures during the loading–unloading cycle, calculated by the molecular dynamics simulations. Snapshots of (c) B2→B19' and (d) B19'→B2 transition under tensile loading. The systems were stretched along the Y-direction, and the strain rates were $5\times10^{8}\ s^{-1}$.

Starting from the B2 structure, the phase transition stress is $\sigma = 13.71\text{GPa}$, shown in **Fig. 5**(a). The strain of phase transition from B2 to B19' structure by calculation is much larger than that by experiments,[13] probably this is the critical phase transition stress without considering the nucleation process which is caused by fluctuation and can significantly reduce the transition stress. Nevertheless, our study of the critical stress can shed some light on the relative barriers of B2→B19' transition, versus B19'→B2 transition. **Fig. 5**(c) shows the snapshots of evolution.

View Article Online
DOI: 10.1039/C7NR04466F

The transition emerges at local domain. The orientation relationship from to B2 structure to the B19' one is: [001] $_{B2}$//[110] $_{B19'}$. In contrast, if we start from B19' structure, the stress of turning point (to B2 structure) is only $\sigma = 2.22\,\mathrm{GPa}$, much lower than that of B2→B19' transition, which is shown in **Fig. 5**(b). Therefore, the B19'→B2 transition is much easier. It will take a much longer path to change the B2 phase to B19' phase, though this is possible as shown in **Fig. 5**(a). Meanwhile the B2→B19' transition occurs at the plastic region, which is also coordinated with previous experimental result that martensitic transition from B2 to B19' can be induced by plastic deformation.[25] **Fig. 5**(d) presents that the orientation relationship in B19'→B2 transition is [001] $_{B19'}$//[011] $_{B2}$. In the B19'→B2 transition, the stress drops from $\sigma = 2.22\,\mathrm{GPa}$ to $\sigma = -6.25\,\mathrm{GPa}$, during the transition. The negative value of stress indicates that after the phase transition, the newly formed B2 phase tends to expand in its length. i.e. the tensile B19' phase transforms to the B2 one which is under compressed state (see details about the size variation during the phase transition in Supporting Information, section SI.4). Under a uniform tensile stress, the sample will suddenly expand in its length. Once the stress reaches $\sigma = 16.22\,\mathrm{GPa}$, the opposite phase transition happens, i.e., from B2 to B19'. Therefore, we found the two-step phase transition (B19'→B2→B19') under uniaxial tensile loading, and the two B19' phases are in different orientations, which is analogous to the experimental results studied by Wang et al.[40] The results show that the B19' phase with low symmetry transforms to the B2 phase with high symmetry under low stress. Once the

View Article Online
DOI: 10.1039/C7NR04466F

stress increases to the critical value, the symmetry breaks and the B2 phase transforms to B19' phase.

From **Fig. 5**(a), it can be observed that the zone of B19'→B2 phase transition is much narrower than that of the B2→B19' phase transition. This is related to the phase selectivity under stress. The process of cyclic deformation on CuZr-based metallic glasses have been studied using experiments[41] and simulations.[42] Herein, to further study the kinetic process of the phase transitions, we have simulated the tensile stress loading-unloading cycles of the two systems, starting from B2 and B19' structures respectively, and the results are shown in **Fig. 5**(a,b). It is shown that B2 transforms to B19' under tension, and then returns to B2 during the process of unloading, qualitatively agreeing with the experimental results studied by Wu et al.[43] Generally, the plastic deformation is irreversible because the defects (such as dislocations and atom vacancies) in the materials play an important role. For MGs, there are many complicated variations during the plastic deformation, including merger of free volume, appearance of shear bands, which make the plasticity irreversible. In our work, we simplified the model and built two perfect crystal supercells for B2 and B19', and did not introduce any defects in the materials. So during unloading, the plastic procedure of the inverse phase transition of B19'→B2 seems to be reversible, as shown in Fig. 5(a). On the other hand, the B19' transforms to B2, keeping the phase structure in a wide strain region during the tension and the whole process of unloading, which agrees well with the conclusion of **Fig. 3** that the B2 structure has a much larger basin of attraction. The results indicate that the B2 structure is much stable than

View Article Online
DOI: 10.1039/C7NR04466F

the B19' structure under strain, which can further explain the experiment that only B2 nanocrystals are observed after tension.

4. Discussion

In the present work, we study the phase selectivity of CuZr depended on heat history and force loading process. The results and the related mechanism are summarized in **Fig. 6**. After slow quenching (~10^2 K/s) from the liquid state, both nanocrystals with B2 and B19' phases are generated, shown in **Fig. 1**(b) and **1**(c). According to the literatures, the B2 CuZr is internal energyless stable and can undergo a martensitic transition to the B19' phase during the quenching. Although the B19' phase is the relative stable phase at the room temperature, with lower thermodynamic energy, the difference of the two phases is not obvious ($\Delta E = 0.022\,\mathrm{eV\,atom^{-1}}$), so they can coexist in the glassy matrix. If the cooling rate is faster (~10^6 K/s), the clusters of these phases could not grow adequately, and the amorphous alloy is obtained. Interestingly, when the CuZr amorphous alloy is stretched uniaxially, only the nanocrystals of B2 structure are generated, with no sign of B19' structure.

View Article Online
DOI: 10.1039/C7NR04466F

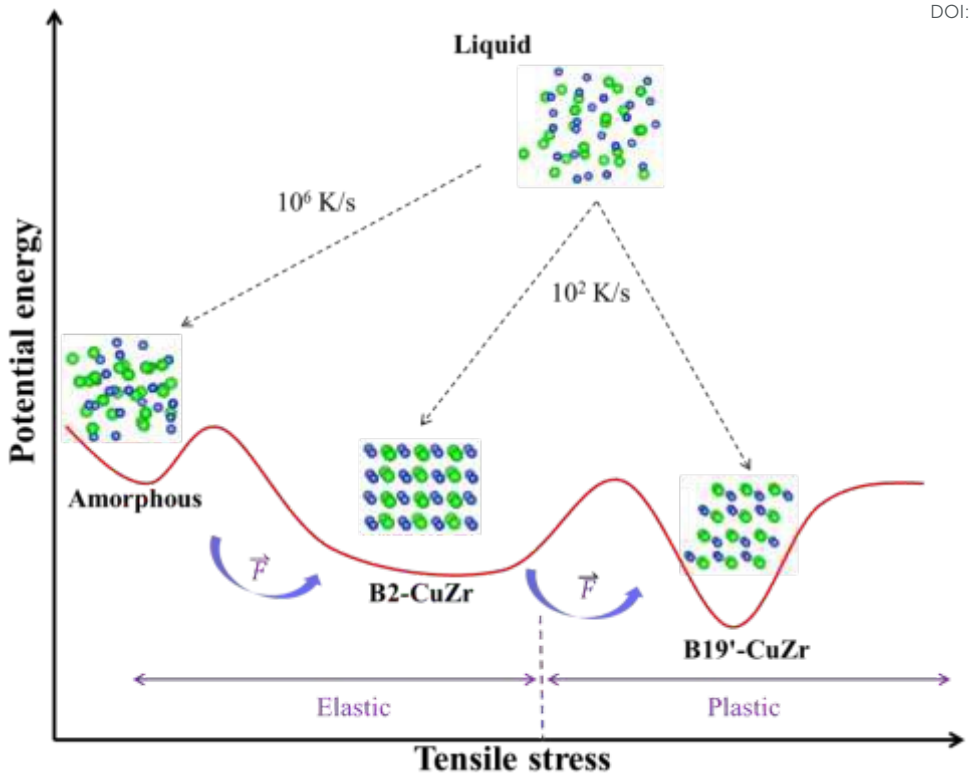

Fig. 6. Schematic of phase selectivity under thermal cooling (differnt quenching speed 10^2 vs.10^6 K/s) and tensile stress ($\vec{F}$ means force). Nanocrystals of B19' and B2 phases are generated from liquid binary CuZr alloy after slow quenching (~10^2 K/s). Only the B2 (thermodynamic metastable phase) nanocrystals are generated from the amorphous matrix (obtained by fast quenching, ~10^6 K/s) under tensile stress, due to the more dynamic stability.

Based on our experimental results, we propose that under the applied uniaxial tensile stress, the short-range topological structures in the amorphous matrix selectively transform to the B2 clusters and then grow into nanocrystals. Although the B19' clusters (if they exist in size smaller than the observable nanocrystals) can be generated during the slow quenching, their clusters are dynamic metastable and easily

View Article Online
DOI: 10.1039/C7NR04466F

transformed to the B2 structures under tension. From the view of thermodynamics, the theoretical calculation of Gibbs free energy judges the probability of B19'→B2 phase transition under tensile stress. From the view of symmetry, the fact of that the electron redistridution of higher symmetric B2 (cubic) structure exhits the isotropic behavior vs. the anisotropy of electron redistridution of lower symmetric B19' (monoclinic) structure indicates that the phase transition under directional stress is accompanied with raising symmetry of phase structure. On the other hand, the MD simulations indicate that the B19' phase is dynamic metastable, and easily transforms to the B2 phase which is stable in a relative large deformed region, i.e. has larger attractive basin. Thus all the results of theoretical calculations support the experimental observations that under tensile stress, only the B2 crystal phase, which have higher crystalline symmetry (cubic) and is the thermodynamic metastable phase, has been generated in CuZr MGs.

5. Conclusion

In summary, we study the phase selectivity of CuZr under tensile stress. Although the B19' phase is the relative stable phase with lower thermodynamic energy, only nanocrystals of B2 structure are generated. All the results of theoretical calculations support the experimental observations that under tensile stress, only the B2 crystal phase, which have higher crystalline symmetry (cubic) and is the thermodynamic metastable phase, has been generated in CuZr metallic glasses. Such mechanism of phase selectivity and phase transformation mechanism under uniaxial

View Article Online
DOI: 10.1039/C7NR04466F

stress not only extends the scope of crystallization in metallic glasses but also can be used in actual material manipulations to yield different phases with related properties.

Conflicts of interest

There are no conflicts of interest to declare.

Acknowledgments

This research was supported by the Guangdong Innovation Team Project (No. 2013N080) and the Shenzhen Science and Technology Research Grant (No. ZDSY20130331145131323). W. Liao gratefully acknowledges the financial support from the Natural Science Foundation of Shenzhen University (Grant No. 2017069) and the Shenzhen Basic Research Project JCYJ20170302142339007.

Appendix A . Supplementary data

Details of the experimental section, measurements and characteristics, and supplementary tables and figures.

References

1 W. L. Johnson, *MRS Bull.*, 1999, **24**, 42-56.

2 M. F. Ashby and A. L. Greer, *Scripta Mater.*, 2006, **54**, 321-326.

3 A. Inoue, *Acta Mater.*, 2000, **48**, 279-306.

4 A. Schuh, T. C. Hufnagel and U. Ramamurty, *Acta Mater.*, 2007, **55**, 4067-4109.

5 F.F. Wu, Z.F. Zhang, S.X. Mao, A. Peker and J. Eckert, *Phys. Rev. B*, 2007, **75**, 134201.

6 Z.F. Zhang, J. Eckert and L. Schultz, Acta Mater., 2003, 51, 1167-1179.

7 J. Das, M.B. Tang, K.B. Kim, R. Theissmann, F. Baier, W.H. Wang and J. Eckert, *Phys. Rev. Lett.*, 2005, **94**, 205501.

8 S. Pauly, S. Gorantla, G. Wang, U. Kühn and J. Eckert, *Nat. Mater.*, 2010, **9**, 473-477.

9 D. Xu, B. Lohwongwatana, G. Duan, W. L. Johnson and C. Garland, *Acta Mater.*, 2004, **52**, 2621-2624.

10 Q. An, K. Samwer, W. A. Goddard, 3rd, W. L. Johnson, A. Jaramillo-Botero, G. Garret and M. D. Demetriou, *J. Phys. Chem. Lett.*, 2012, **3**, 3143-3148.

11 S. Q. Jiang, Z. W. Wu and M. Z. Li, *J. Chem. Phys.*, 2016, **144**, 154502.

12 S. Pauly, G. Liu, G. Wang, J. Das, K. B. Kim, U. Kühn, D. H. Kim and J. Eckert, *Appl. Phys. Lett.*, 2009, **95**, 101906.

13 S. Pauly, J. Das, J. Bednarcik, N. Mattern, K. Kim, D. Kim and J. Eckert, *Scripta Mater.*, 2009, **60**, 431-434.

14 K. Lu, *Mat. Sci. Eng. R.*, 1996, **16**, 161-221.

15 R. Wei, Y. Chang, Y. F. Li, G. Li, S. Yang, C. J. Zhang and L. He, *Mater. Sci. Eng. A*, 2013, **587**, 233-239.

16 W. Qin and Z. H. Chen, *J. Alloys Compd.*, 2001, **322**, 286-289.

17 Q. Meng, N. Zhou, Y. Rong, S. Chen, T. Y. Hsu and X. Zuyao, *Acta Mater.*, 2002, **50**, 4563-4570.

18 T. Waitz, K. Tsuchiya, T. Antretter and F. D. Fischer, *MRS Bull.*, 2009, **34**, 814-821.

19 I. W. Chen, Y. H. Chiao and K. Tsuzaki, *Acta Metall.*, 1985, **33**, 1847-1859.

20 T. Waitz, T. Antretter, F. D. Fischer and H. P. Karnthaler, *Mater. Sci. Technol.*, 2008, **24**, 934-940.

21 A. Ahadi and Q. Sun, *Acta Mater.*, 2015, **90**, 272-281.

22 W.-S. Ko, S. B. Maisel, B. Grabowski, J. B. Jeon and J. Neugebauer, *Acta Mater.*, 2017, **123**, 90-101.

23 M. A. Azeem and D. Dye, *J. Alloys Compd.*, 2015, **618**, 469-474.

24 Y. Wu, H. Wang, H. H. Wu, Z. Y. Zhang, X. D. Hui, G. L. Chen, D. Ma, X. L. Wang and Z. P. Lu, *Acta Mater.*, 2011, **59**, 2928-2936.

25 Y. Wu, Y. Xiao, G. Chen, C. T. Liu and Z. Lu, *Adv. Mater.*, 2010, **22**, 2770-2773.

26 Y. Q. Cheng, A. J. Cao, H. W. Sheng and E. Ma, *Acta Mater.*, 2008, **56**, 5263-5275.

27 W. Liao, J. Hu and Y. Zhang, *Intermetallics*, 2012, **20**, 82-86.

28 M. I. Mendelev, M. J. Kramer, R. T. Ott, D. J. Sordelet, D. Yagodin and P. Popel, *Philos. Mag.*, 2009, **89**, 967-987.

29 Y. Q. Cheng, A. J. Cao and E. Ma, *Acta Mater.*, 2009, **57**, 3253-3267.

30 X. H. Lin and W. L. Johnson, *J. Appl. Phys.*, 1995, **78**, 6514-6519.

31 H. Wagner, D. Bedorf, S. Küchemann, M. Schwabe, B. Zhang, W. Arnold and K. Samwer, *Nature Mater.*, 2011, **10**, 439-442.

32 J. L. Finney, *P. Roy. Soc. A*, 1970, **319**, 479-493.

View Article Online
DOI: 10.1039/C7NR04466F

33 M. T. Yin and M. L. Cohen, *Phys. Rev. Lett.*, 1983, **50**, 2006-2009.

34 R. J. Needs and R. M. Martin, *Phys. Rev. B*, 1984, **30**, 5390-5392.

35 C. Cheng, W. H. Huang and H. J. Li, *Phys. Rev. B*, 2001, **63**, 153202.

36 M. Chen, *Annu. Rev. Mater. Res.*, 2008, **38**, 445-469.

37 Q. S. Zeng, Y. Ding, W. L. Mao, W. Yang, S. V. Sinogeikin, J. Shu, H. K. Mao and J. Z. Jiang, *Phys. Rev. Lett.*, 2010, **104**, 105702.

38 X. F. Wang, T. E. Jones, Y. Wu, Z. P. Lu, S. Halas, T. Durakiewicz and M. E. Eberhart, *J. Chem. Phys.*, 2014, **141**, 024503.

39 X. L. Wang, J. Almer, C. T. Liu, Y. D. Wang, J. K. Zhao, A. D. Stoica, D. R. Haeffner and W. H. Wang, *Phys. Rev. Lett.*, 2003, **91**, 265501.

40 S. J. Wang, H. Wang, K. Du, W. Zhang, M. L. Sui and S. X. Mao, *Nat Commun*, 2014, **5**, 3433.

41 D. Jang, R. Maaß, G. Wang, P. K. Liaw and J. R. Greer, *Scripta Mater.*, 2013, **68**, 773-776.

42 Z. D. Sha, S. X. Qu, Z. S. Liu, T. J. Wang and H. Gao, *Nano Lett.*, 2015, **15**, 7010-7015.

43 F. F. Wu, K. C. Chan, S. S. Jiang, S. H. Chen and G. Wang, *Sci Rep*, 2014, **4**, 5302.

View Article Online
DOI: 10.1039/C7NR04466F

Table of Contents

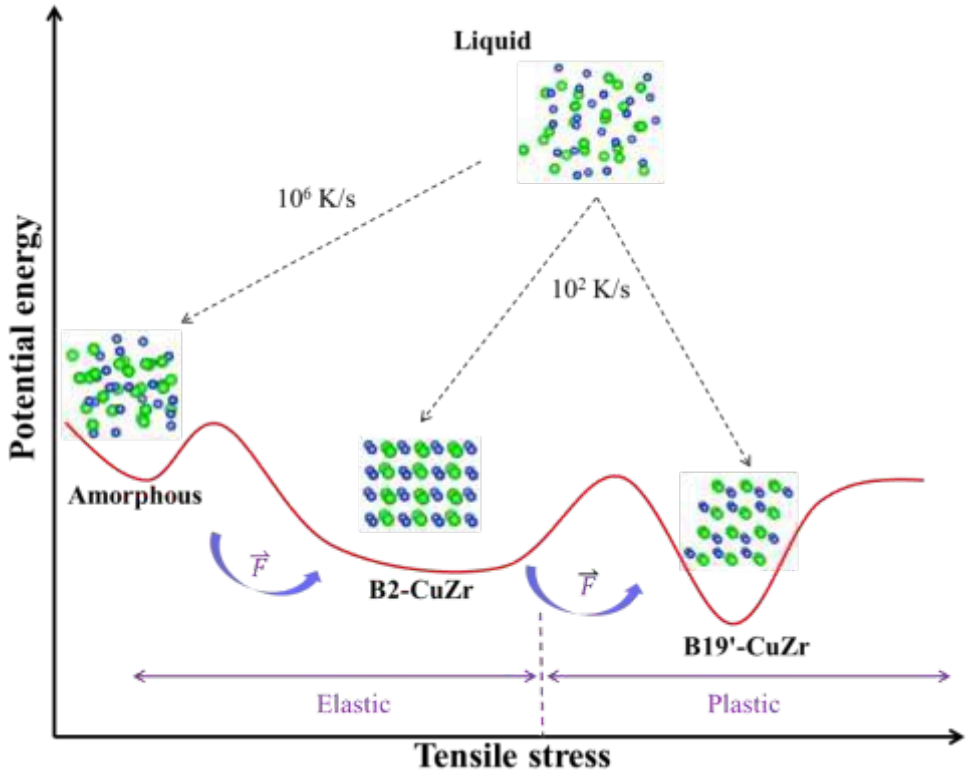

Nanocrystals with the B2 structure are generated from the CuZr glassy fiber and the mechanism of phase selectivity is revealed.